

The structure and dynamics of NGC 1333 from ^{13}CO and C^{18}O observations.

S. Warin¹, A. Castets¹, W.D. Langer², R.W. Wilson³, and L. Pagani⁴

¹Laboratoire d'Astrophysique, Observatoire de Grenoble, B.P.53X, F-3 8041, Grenoble Cedex 9, France

²MS 169-506, Jet Propulsion Laboratory, Pasadena, CA 91109, USA

³AT&T Bell Laboratories, 11031-1,245, Holmdel, NJ 07733, USA

⁴DEMIRM, Observatoire de Paris, 61 avenue de l'Observatoire, F-75014 Paris, France

Received, accepted

Abstract. This paper presents a study of a dense molecular region, NGC 1333, and the relationship of the embedded infrared sources and young stellar objects to the structure of its molecular core. We use ^{13}CO and C^{18}O $J=1\rightarrow 0$ and $J=2\rightarrow 1$ observations, along with those of $\text{CS } J=2\rightarrow 1$ to characterize the structure of the core, calculate densities and masses. We find from our C^{18}O maps that the core consists of a cavity surrounded by a compressed shell of gas. Many of the infrared and outflow sources in NGC 1333 are located in the cavity and the outflow winds from IRAS2, SSV 13 and several other sources appear to be responsible for creating the cavity and forming the shell. We suggest that sequential star formation is taking place in NGC 1333 with successive generations of young stellar objects providing the energy to expand the cavity, sweep up the material and compress the shell. Several massive. ($\sim 20 - 40 M_{\odot}$) condensations in the shell are potential sites for the next generation of star formation in NGC 1333.

Key words: star: formation-ISM: clouds-ISM: molecules-ISM: structure-ISM: kinematics and dynamics-ISM: individual objects: NGC 1333

1. Introduction

NGC 1333 is a cloud in the Perseus complex with an active star forming core. It contains numerous infrared sources, Herbig-Haro objects, H_2O masers, $\text{H}\alpha$ stars and outflows. In this paper we study the large scale structure of the core using multi-transition maps of CO isotopes and a single transition of CS ($J=2\rightarrow 1$) and discuss the relationship of the embedded stellar objects with this structure.

Send offprint requests to: S. Warin

1.1. The Perseus complex

The Perseus molecular complex is a conglomeration of regions of high visual extinction extending over some 9 by 9 degrees at a galactic longitude of $\sim 160^\circ$ and latitude $\sim -19^\circ$. Its high galactic latitude and its low LSR velocity determined from CO (Sargent 1979) and ^{13}CO (Bachiller & Cernicharo 1986) suggest that it is within a few hundred parsecs from the sun although its exact distance remains somewhat controversial. Most authors agree that the Perseus group is associated with the Per OB2 association. The question of the distance to the Perseus complex has been debated by several authors (Bergman and Blaauw (1964); Strom et al. 1974; Cernicharo et al. 1985). The current consensus is that the Per OB2 association is at 300 pc and the NGC 1333 cloud somewhat farther away. Following Ladd et al. (1993) we adopt 350 pc as the distance to NGC 1333.

The Perseus complex contains two active sites of star formation, IC 348 and NGC 1333, connected by a chain of colder dark clouds (e.g. B 1, B 1 E) with strong molecular emission. These two active regions contain newly-formed intermediate-mass stars of spectral type B, as well as a cluster of young stars of lower mass. While the creation of Per OB2 and IC 348 has been more or less concurrent, they have a common age of a few million years (Bergman and Blaauw 1964), in NGC 1333 star formation has taken place only within the last 10^5 years (Sargent 1979). This group of molecular clouds differs in many respects from the Taurus and Orion clouds. Unlike the Taurus and Auriga clouds, where only T-Tauri stars are found, young stars with relatively high luminosity are associated with the Perseus complex. Furthermore from an infrared study of embedded young stars, Ladd et al. (1993) concluded that Perseus differs significantly from Taurus in its concentration of star formation in only two clusters, NGC 1333 and IC 348. Thus, Perseus can perhaps be viewed as a smaller and less populous version of L 1641 (a molecular cloud associated with the Trapezium cluster and containing Orion) with both isolated and cluster star formation (Ladd et al. 1993). In addition almost all the Perseus IRAS sources appear to be individual sources while in L 1641 IRAS sources are associated with multiple infrared sources and may contain small stellar clusters (Strom et al., 1989). Furthermore early spectral type O stars which are usually found in the giant molecular clouds, are not associated with the star formation regions in Perseus.

The whole Perseus complex has been surveyed at low resolution in the $^{12}\text{CO } J=1\rightarrow 0$ molecular emission line with a resolution of $2.5'$ and a sparse sampling of $10'$ (Sargent 1979) and a resolution of $30'$ (Ungerrechts and Thaddeus 1985). Bachiller and Cernicharo (1986) mapped Perseus in $^{13}\text{CO } J=1\rightarrow 0$ with $5'$ resolution. From star counts Cernicharo et al. (1985) derived a total mass of gas of $2 \times 10^4 M_\odot$ for the Perseus cloud complex (including both atomic and molecular gas).

1.2. The NGC 1333 star forming region

The NGC 1333 star formation region has been extensively studied in the past both in the millimeter and centimeter molecular lines and in the infrared continuum emission. Lada et al (1974) derived a mass of $10^3 M_\odot$, with $n(\text{H}_2) \geq 10^4 \text{ cm}^{-3}$ and $T_k \sim 20$ K over most of the NGC 1333 core using HCN, CS and NH_3 to trace the dense gas. This temperature and density agree with those derived by Schwartz et al. (1978) using a low resolution NH_3 survey. Schwartz et al. also found that the H_2CO and CS 2111111 lines peak at the location of the infrared sources reported by Strom et al. (1974). NGC 1333 has also been mapped at moderate resolution ($2.6'$) by Loren (1976), in the HCO^+ and $^{13}\text{CO } J=1\rightarrow 0$ emission lines, on a grid with a $2'$ spacing for the central part, and with a larger spacing ($6'$) around the center. Loren concluded from the ^{12}CO line shape that star formation in NGC 1333

has been initiated by a cloud-cloud collision followed by collapse. This conclusion was ruled out by Ho and Barrett (1980) who used a slightly higher angular resolution ($85''$) NH_3 and ($23''$) ^{13}CO survey of the cloud to propose an alternative picture of dense fragments embedded in a lower density cloud.

In addition to the near-IR imaging photometry at 1.65 and 2.2 μm by Ladd et al. (1993), infrared surveys of NGC 1333 consist of J, H, K and L photometry by Strom et al. (1976) and Aspin et al. (1994) and the far-IR observations of Harvey et al. (1984) and Jennings et al. (1987). In NGC1333, Strom et al. (1976) discovered 25 embedded sources, a number which was raised recently to 100 (Aspin et al. 1994). Some of these embedded sources were also seen at 100 μm by Harvey et al. while Jennings et al. using IRASPC observations found five more far-IR sources. NGC1333 has also been the subject of selected radio and/or infrared observations devoted to the objects found in the central part of this star-forming cluster: T-Tauri stars, infrared sources (SGS 1: Castelar et al. 1986; IRAS 4: Sandell et al. 1991; SVS 13: Liseau et al. 1992; Bregman et al. 1993) and Herbig-Haro objects with their exciting sources (HH 4 to HH 18, the most studied being HH 7-11; see a complete reference list in Reipurth 1994). Many of these studies concentrate particularly on the HH7-11 spectacular molecular outflow (Snell and Edwards 1981; Schwartz et al. 1983; Edwards and Snell 1984; Liseau et al. 1988; Lizano et al. 1988; Phillips and Mampaso 1990; Bachiller and Cernicharo 1990; Dent et al. 1993) driven by the SSV 13 source. Depending on the spatial resolution and on the sensitivity of the observations the velocity of this outflow was first found to extend from -20 to +25 km s^{-1} (Snell and Edwards 1981) with a momentum, kinetic energy and mass loss rate of $11\text{M}_{\odot}\text{K}\cdot\text{km s}^{-1}$, 4×10^{46} ergs, and $8 \times 10^{-6}\text{M}_{\odot}\text{yr}^{-1}$ respectively. In 1988 Liseau et al. suggested that there was not one but a cluster of outflows which confuses the identification of the driving source. In addition recent observations by Lizano et al. (1988) and Bachiller and Cernicharo (1990) showed the presence of a well collimated extremely high velocity outflow with a terminal velocity of 160 km s^{-1} . According to Bachiller and Cernicharo this fast outflow is accelerated by the jet-like gas emanating from the central source and will undergo braking processes (shocks, compression) at the interface zone with the ambient cloud. Furthermore, the high velocity, highly collimated outflow produces the lower velocity, broader outflow seen in ^{13}CO .

Here we will show that these embedded sources and their associated outflows have had a profound effect on the structure of the core in NGC 1333. They are responsible for the generation of a large bubble (or cavity) with a compressed shell at its boundary. Several massive clumps in this shell are gravitationally bound and unstable to collapse, and may be the source of the next generation of young stellar objects in NGC 1333. Taken all together the existing IR and outflow sources, the cavity and shell suggest a history of shock driven sequential star formation that is still ongoing in NGC 1333.

2. Data acquisition

The results presented here are based on $J = 1 \rightarrow 0$ ^{13}CO and C^{18}O and $J = 2 \rightarrow 1$ ^{13}CO observations made with the AT&T Bell Laboratories 7-meter antenna in Holmdel, NJ (hereafter BL), and on $J = 2 \rightarrow 1$ ^{13}CO and C^{18}O data obtained with the 2.5 meter POM-2 telescope located on the Plateau de Burt in France. The beam of the BL antenna at the $J = 1 \rightarrow 0$ ^{13}CO frequency is about $1''$, somewhat smaller than the $140''$ POM-2 beam used for the $J = 2 \rightarrow 1$ observations.

The $J = 1 \rightarrow 0$ C^{18}O observations were made in winter 1992 and 1993. The $J = 1 \rightarrow 0$ ^{13}CO spectra were extracted from an unpublished Bell Labs survey of Perseus (Langer and Wilson). The single side band (SSB) system temperatures (including sky

and forward efficiency corrections) varied from 200 to 400 K depending on elevation and weather conditions. All the ^{13}CO , C^{18}O and CS spectra were obtained using a frequency switching mode. Additional details on the receiver, calibration and observing procedures are given in Bally et al. (1987) and Langer et al. (1989). The spectral resolution of the observations was 50 kHz (0.14 km s^{-1}) for C^{18}O and CS, and 100 kHz (0.27 km s^{-1}) for ^{13}CO . The central position ($\alpha(1950) = 3^{\text{h}} 41^{\text{m}} 29.0^{\text{s}}$, $\delta(1950) = 32^{\circ} 44' 30''$) was monitored regularly during the observations to check calibration (Langer et al. 1989). The average channel to channel rms noise is 0.3 K for all the observations, except at the center of the C^{18}O map where we integrated longer to obtain 0.15 K. The ^{13}CO map covers $50' \times 90'$ in right ascension (α) and in declination (δ) and the C^{18}O map covers $50' \times 65'$. The Bell Labs maps are spatially sampled every $1'$ (nearly at the Nyquist sampling rate) and are centered at $\alpha(1950) = 3^{\text{h}} 25^{\text{m}} 56.5^{\text{s}}$, $\delta(1950) = 31^{\circ} 10' 14''$, and a $V_{\text{LSR}} = 7 \text{ km s}^{-1}$.

The CS $J = 2 \rightarrow 1$ map of the NGC1333 cloud was made with the BL 7 meter antenna in January 1993 with a $1'$ sampling. The spectral resolution of these data is 100 kHz (0.3 km s^{-1}) and the channel to channel rms noise is about 0.1 K for the central part and 0.3 K elsewhere. The CS map covers an area of $20' \times 50'$, a slightly smaller area than the C^{18}O map. These CS observations serve as a high density gas tracer of the internal structure of the cloud.

The CO $J = 2 \rightarrow 1$ observations were made during winter 1993 and 1994 with the POM-2 antenna. General information about the POM-2 telescope is given in Castets et al. (1988) but a number of changes have been made in the system since then. In 1992 our Schottky barrier diode receiver was replaced by an SIS receiver housed in a closed-loop cryogenerator. This SIS receiver has excellent performance ($T_{\text{rec}}(\text{DSB}) \simeq 70 \text{ K}$) in the range 210-250 GHz. The calibration is achieved by chopping between two loads at different temperature. During the observations the system temperature varied from 400 to 1200 K corresponding to a water vapor variation of 0.5 to 3 mm of precipitable water ($\tau = 0.05$ to 0.3). The forward and beam efficiencies were also improved since 1988 to $\eta_f = 0.82$ and $\eta_{f,s} = 0.68$ respectively. The absolute pointing error, checked on Jupiter is about $15''$ and always less than $20''$. All $J = 2 \rightarrow 1$ spectra were obtained using a position switching mode with the reference position equal to ($0^{\circ}, 120'$) about the NGC 1333 center. The spectral resolution was 156 kHz (0.2 km s^{-1}) for both ^{13}CO and the C^{18}O observations. Under these conditions we had an average channel to channel rms noise of 0.3 K for all spectra. The ^{13}CO and C^{18}O $J = 2 \rightarrow 1$ maps were observed on a $1.25'$ grid (Nyquist sampled) and covering an area of $43' \times 87'$ and $25' \times 50'$, respectively. All molecular data have been corrected for atmospheric absorption and for the antenna main beam efficiency and the values for line intensities given in this paper are radiation temperature T_{r} .

3. Results

In this section we present and analyse ^{13}CO , C^{18}O and CS maps from which we will derive the overall structure, density and mass of the NGC1333 core. First we discuss the integrated intensity maps and then the individual velocity channel maps. Second we use an LVG model to interpret the CO data and derive physical parameters for the core.

3.1. Spatial Maps

In Fig. 1 we present the ^{13}CO velocity integrated intensities for the $J = 1 \rightarrow 0$ and $J = 2 \rightarrow 1$ transitions. The two ^{13}CO maps are very similar in shape and show that the NGC 1333 cloud has two major features: 1) a large elliptical core oriented NE-SW

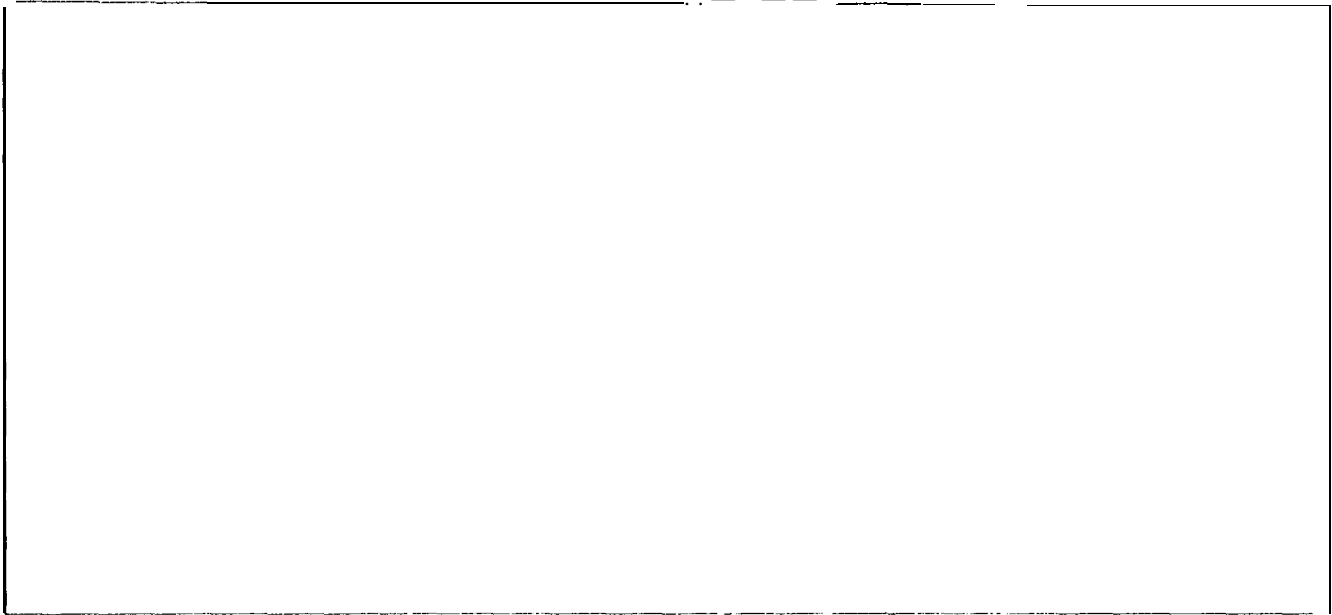


Fig. 1, Integrated velocity maps for the $J = 1 \rightarrow 0$ (left) and $J = 2 \rightarrow 1$ (right) transitions of ^{13}CO . The interval of integration in LSR-velocity is 4 to 10 km s^{-1} . The $J = 1 \rightarrow 0$ was obtained with the AT&T Bell Laboratories 7-meter antenna and the $J = 2 \rightarrow 1$ with the 2.5 meter POM-2 telescope located on the Plateau de Bure, France. In both maps contours levels range from 1 to 33.5 K km s^{-1} incremented by 2.5 K km s^{-1} . Positional offsets are in arcminutes relative to: $\alpha_{1950} = 3^{\text{h}} 25^{\text{m}} 56.5^{\text{s}}$, and $\delta_{1950} = 31^{\circ} 10' 14''$.

along the major axis (diameters of the minor x major axes $\sim 17' \times 25'$ corresponding to the size of the 11 K km s^{-1} contour) centered at the position $(2', -3')$; and 2) an elongated structure to the south, an “elephant trunk” filament, which connects with the L1455 cloud (cf. Bachiller and Cernicharo, 1986).

In Fig. 2, we present the $\text{C}^{18}\text{O } J = 1 \rightarrow 0$ and $J = 2 \rightarrow 1$ velocity integrated area maps. In the $J = 1 \rightarrow 0$ line the C^{18}O emission also traces the elliptical core and the filament. However the size of the core is slightly smaller than the one delineated in ^{13}CO ; it extends from $5'$ to $-8'$ in RA and from $-15'$ to $5'$ in declination (size $\sim 13' \times 20'$). The C^{18}O core boundary corresponds roughly to the 16 K km s^{-1} contour in the $^{13}\text{CO } J = 1 \rightarrow 0$ map (Fig. 1). Furthermore this C^{18}O core has a very peculiar “C” shaped appearance, i.e. an almost circular ring of material with a hole in the middle and at least three subcores can be distinguished in this “C” shell. These features are not seen in the ^{13}CO map and, as will be discussed below, this “C” structure is a projection of a nearly spherical (or perhaps spherical) shell surrounding a cavity to form a “limb brightened” edge. Almost all the infrared sources and Herbig-Haro objects which have been discovered in the NGC 1333 cloud are associated with or inside this “C” shaped feature. In particular the SSV13 source and its associated HH7-11 objects lie in the central hole at the boundary with the shell, while the red lobe associated with its high velocity outflow fills the cavity. In Fig. 2 we have indicated the position of these sources (Jennings 1987; Gezari et al. 1993) and traced the blue and red lobes of the outflow observed by Snell and Edwards (1981). In the $\text{C}^{18}\text{O } J = 2 \rightarrow 1$ line the emission covers the same area as the $J = 1 \rightarrow 0$ line but with a more patchy appearance due to the larger spatial resolution, coarser sampling and poorer signal to noise of the spectra. The “C” feature in $\text{C}^{18}\text{O } J = 2 \rightarrow 1$ is less conspicuous than in $\text{C}^{18}\text{O } J = 1 \rightarrow 0$ because the opacity of the $J = 2 \rightarrow 1$ line ($\tau_{21} \geq 1$) is twice that of the $J = 1 \rightarrow 0$, although the three subcores and a curved bridge of material which link them can still be seen in the map.

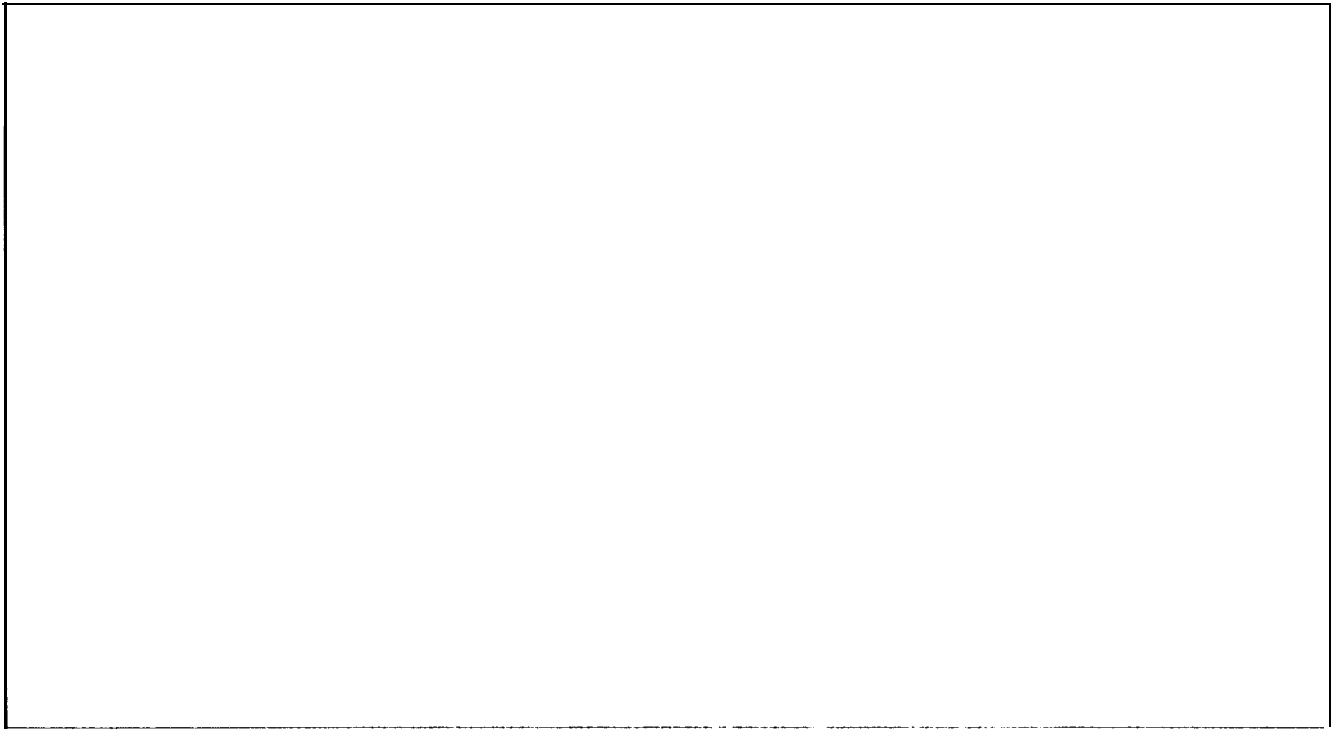


Fig. 2. Integrated velocity maps for the $J = 1 \rightarrow 0$ (left) and $J = 2 \rightarrow 1$ (right) transitions of C^{18}O . The interval of integration in LSR-velocity is from 4 to 10 km s^{-1} . The $J = 1 \rightarrow 0$ was obtained with the AT&T Bell Laboratories 7-meter antenna and the $J = 2 \rightarrow 1$ with the 2.5 meter POM-2 telescope located on the Plateau de Burt, France. In both maps contours levels range from 0.2 to 5 K km s^{-1} incremented by 0.4 K km s^{-1} . Positional offsets are in arcminutes relative to the same center as in Fig. 1. Filled circles denote the IRAS sources positions (Jennings et al. 1987) and filled squares the infrared sources with optical counterparts (Strom et al 1976; Gezari et al 1993)

Figure 5 presents the $\text{CS}(J = 2 \rightarrow 1)$ integrated intensity map. The CS emission map shows two peaks separated by a hole. The strongest peak to the south-east coincides with the SSV13 cluster of sources, situated at the edge of the cavity inside the “C” feature seen in C^{18}O , while the second peak corresponds to the northern subcore of this “C” shell. The hole located between the two peaks coincide with the cavity seen in C^{18}O .

3.2, Velocity structure

Apart from the region where the core and the filament merge, all spectra are composed of one velocity component. In the merged region (situated around $-20'$ in declination) the spectra show a blending of two emission features, one from the core and the other from the southern filament.

In Fig. 3 we show the $^{13}\text{CO } J = 1 \rightarrow 0$ integrated intensity in 1 km s^{-1} velocity bins. In this figure the difference between the central velocity of the core and the filament (8 km s^{-1} for the core and 5.5 km s^{-1} for the filament) makes the spatial and structural separation between the core and filament even clearer. In the south, emission from the filament is visible mainly from 5 to 7 km s^{-1} , while in the north the core is seen from 6 to 10 km s^{-1} (the separation between north and south occurs at the $-20'$ offset in declination). The $^{13}\text{CO } J = 2 \rightarrow 1$ velocity structure (not shown) is very similar to that of $J = 1 \rightarrow 0$.

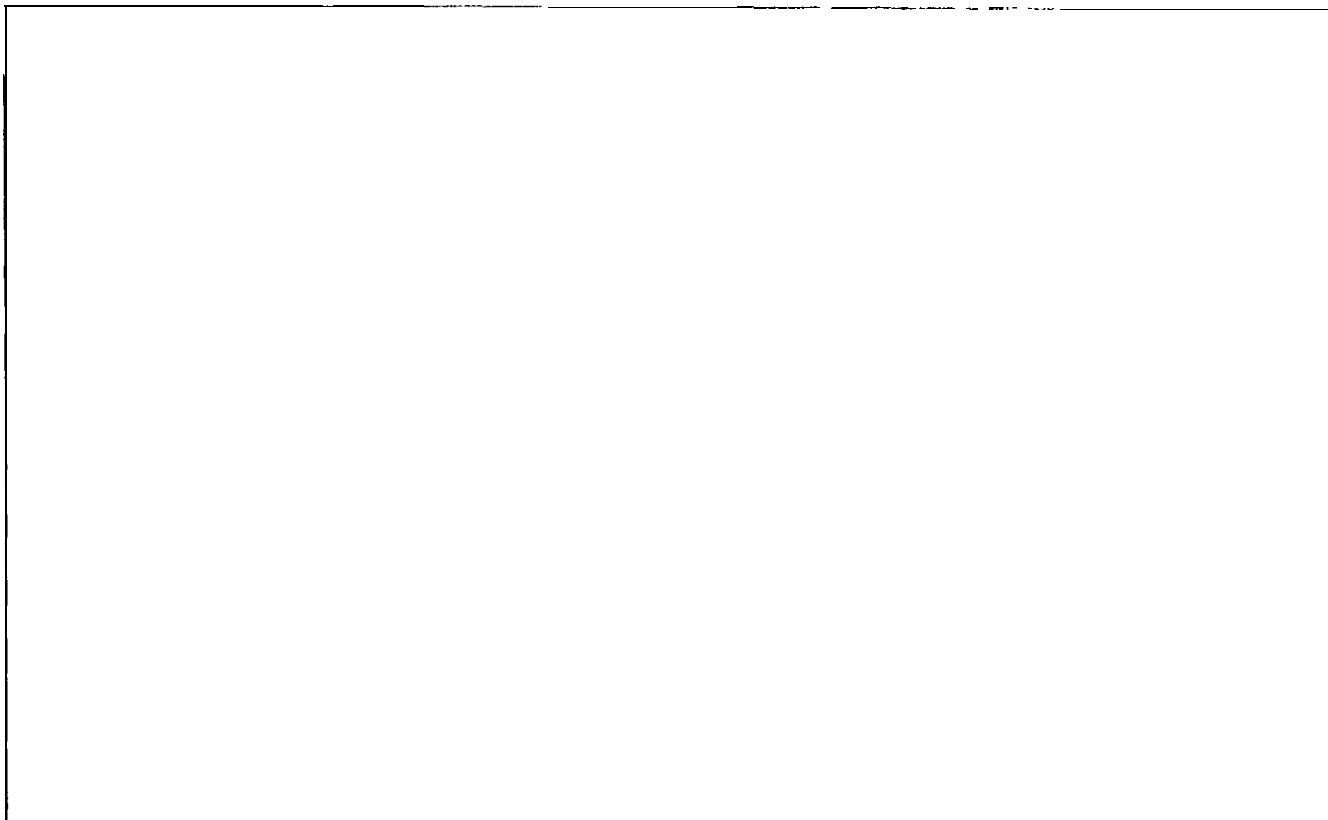


Fig. 3. Channel maps of the NGC 1333 ^{13}CO $J = 1 \rightarrow 0$ emission. The contours are in steps of 1 K from 2 to 16 K, in units of radiation temperature., averaged over 1 km s^{-1} wide channels, centered at $V_{\text{LSR}} = 4.5, 5.5, 6.5, 7.5, 8.5$ and 9.5 km s^{-1} respectively

The C^{18}O $J = 1 \rightarrow 0$ and $J = 2 \rightarrow 1$ velocity maps, unlike that of ^{13}CO , reveal the internal structure of the core. As these two transitions approximately trace the same gas we present in Fig. 4 only the $J = 1 \rightarrow 0$ velocity bins because they have better spatial sampling, higher signal to noise and are more optically thin. In Fig. 4 the intensity map at the $8\text{--}9 \text{ km s}^{-1}$ velocity interval reveals an annulus structure, centered at $(-2', -2')$, with an inner and outer radius equal to $3'$ (0.3 pc) and $6'$ (0.6 pc) respectively. Three subcores can be seen in this annulus structure at $8\text{--}9 \text{ km s}^{-1}$ concentrated in the eastern half of the annulus. The northern and southern subcores can be followed up in the $7\text{--}8 \text{ km s}^{-1}$ map. The cavity which lies between these two subcores is open to the west and slightly open to the east in the ambient cloud. In the $6\text{--}7 \text{ km s}^{-1}$ velocity map the eastern and southern parts of the annulus are still visible while the cavity is opened to the north and west. It can also be seen that the southern filament is connected to the annulus at the southern subcore. In the $9\text{--}10 \text{ km s}^{-1}$ velocity map the eastern subcore is the *only* remaining part of the annulus structure.

The $\text{CS}(J = 2 \rightarrow 1)$ velocity emission maps (see Fig. 5) shows the presence of two bright spots centered at offset of $(0', -5')$ and $(-1', 0')$. The first one corresponds to the SSV1 3 cluster of sources and the second one to the internal side of the northern part of the annulus seen in C^{18}O . Between these two dense "CS" cores we see evidence of the cavity first seen in C^{18}O . The annulus is also delineated in the $8\text{--}9$ and $7\text{--}8 \text{ km s}^{-1}$ velocity bin intervals where both cores are visible,

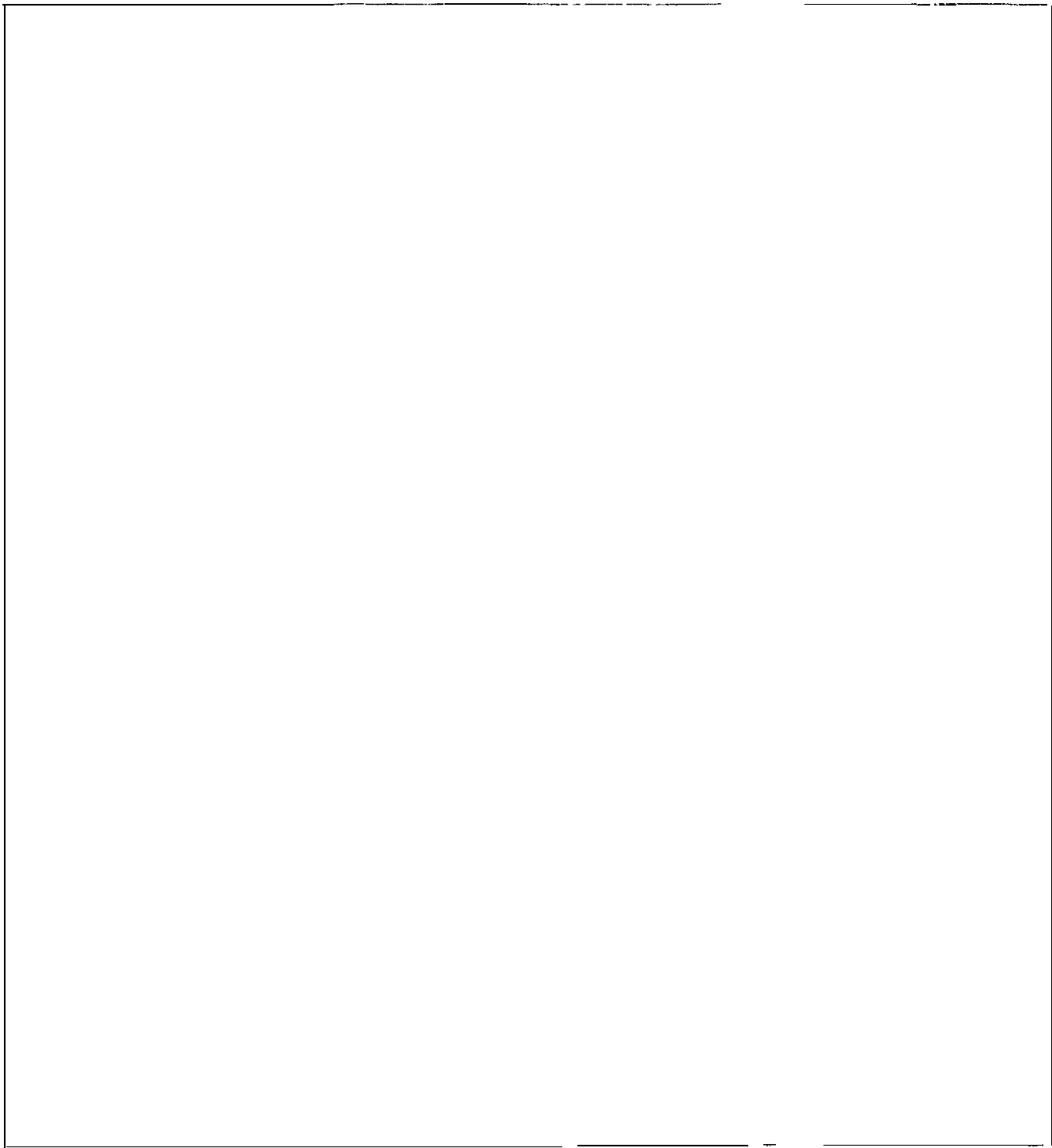


Fig. 4. Channel maps of the NGC1333 C^{18}O $J=1\rightarrow 0$ emission. The contours are in steps of 0.15 K from 0.15 to 1.65 K, in units of radiation temperature, averaged over 1 km s^{-1} wide channels, centered at $V_{lsr} = 4.5, 5.5, 6.5, 7.5, 8.5$ and 9.5 km s^{-1} respectively

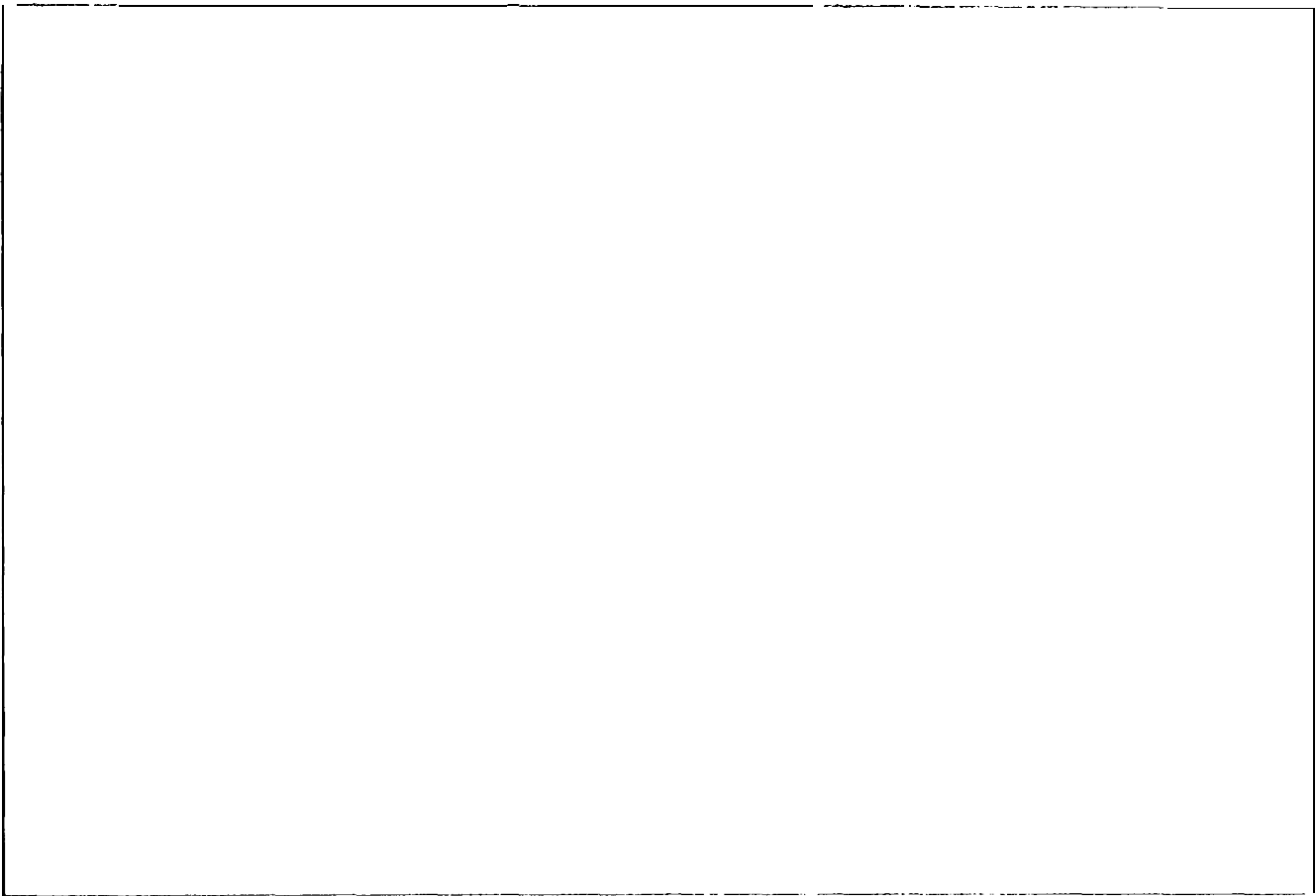


Fig. 5. The top left figure shows the integrated velocity maps for the $J = 2 \rightarrow 1$ transition of CS. The interval of integration in LSR-velocity is from 40.3 to 10.3 km s^{-1} . Contour levels range from 1 to 8 K km s^{-1} incremented by 0.5 K km s^{-1} . Positional offsets in arcminutes are relative to the same center as in Fig. 1. Other figures show channel maps of the NGC 1333 CS $J = 2 \rightarrow 1$ emission. The contours are in steps of 0.25 K from 0.1 to 3.6 K, averaged over 1 km s^{-1} wide channels, centered at V_{LSR} , 5.5, 6.5, 7.5, 8.5 and 9.5 km s^{-1} respectively.

Comparing our CS ($J = 2 \rightarrow 1$) integrated intensity maps with those obtained by Schwartz et al. (1983) in CS ($J = 3 \rightarrow 2$) we see that the CS ($J = 3 \rightarrow 2$) coincides with our CS ($J = 2 \rightarrow 1$) emission. The only obvious difference is the presence on their map of a third peak, probably unresolved in our data (the beam is $50''$ for the observation by Schwartz et al and $120''$ for our observations). Ho and Barrett (1980) mapped NH_3 emission over $6' \times 8'$ in NGC 1333, centered in the same region as the CS and C^{18}O emission. The NH_3 contour map has the same shape as that of C^{18}O , suggesting that the “C”-shell is a region with an enhanced density (Fig. 9). No NH_3 was detected in the cavity as defined by our C^{18}O and CS observations.

All these spatial-velocity features can be explained by the existence of an expanding hollow spherical shell. One side of the shell is closer to the edge of the ambient cloud (to the west) and may be breaking out to the edge of the denser part of the cloud (as traced by C^{18}O anti- ^{13}CO) into the less dense part of the cloud as traced by ^{13}CO . A coarsely sampled map (every $4'$) of ^{12}CO (Langer private communication) does not show any opening at the outermost northeastern edge of the molecular cloud. Thus the expanding cavity has not broken out of the edge of the NGC 1333 cloud. This explanation is supported by the ^{13}CO velocity map at $6\text{--}7 \text{ km s}^{-1}$ which shows the same opening to the west of the $(-2', -2')$ position.

3.3. Physical properties from LVG analysis

Here we use the LVG model described in the appendix of Castets et al. (1990) to derive the C^{18}O and ^{13}CO column densities and H_2 volume densities of the NGC1333 cloud. We assumed a spherical geometry and used the CO collision rates of Flower and Launay (1985) with a H_2 ortho-to-para ratio of 0.25. The LVG approximation is better than LTE since it does not assume thermalized levels and instead determines the excitation temperatures directly from the different transitions.

As the NGC1333 star formation region includes several embedded stars which heat the gas locally we decided to adopt for the kinetic temperature a model in which the central part of the cloud and the periphery have different temperatures. The central region, which includes the HH objects and IR sources, is located between $-4'$ and $10'$ in RA and between $-12'$ and $6'$ in DEC. In the core of this region, we use a kinetic temperature of 18 K, a value obtained by Lada et al. (1974) from NH_3 observations. Outside the core, but still in the direction of the central region, ^{12}CO observations suggest a lower limit for the kinetic temperature which is also 18 K. While the relatively high core temperature is naturally due to the heating by the embedded sources, the also high envelope temperature is probably due to the heating by young sources located outside of the cloud. In the periphery of the cloud, in the absence of embedded IR sources the temperature drops to standard values appropriate to deep in the interior of a cloud which is shielded from the intense UV field. Thus C^{18}O observations have been modeled with $T_{\text{kin}} = 10$ K while ^{13}CO , being optically thick and coming closer to the UV irradiated surface, is slightly warmer. ^{13}CO observations in those parts of the cloud suggest $T_{\text{kin}} = 13$ K which we adopted to model ^{13}CO .

All the excitation calculations were made with the $J = 1 \rightarrow 0$ data resampled to the $J = 2 \rightarrow 1$ resolution. To check the relative calibration and intensities scales of the BL and POM-2 telescopes and to resample the $J = 1 \rightarrow 0$ and $J = 2 \rightarrow 1$ data to the same spatial and velocity resolution ($140''$ and 0.2 km s^{-1}), we followed the method described in Castets et al. (1990) for Orion. The parameters of each spectrum were analyzed using a gaussian fit. Most of the C^{18}O spectra are single peaked with an average width of 1.5 km s^{-1} in the central region and 1 km s^{-1} in the periphery. Several ^{13}CO spectra had a more complex velocity structure. However the additional components are mainly located outside the velocity range of the main peak and have a negligible area. The average linewidth of the ^{13}CO main velocity component are 2.3 and 1.9 km s^{-1} in the central and periphery regions respectively.

The total ^{13}CO and C^{18}O column density obtained with the $J = 1 \rightarrow 0$ and $J = 2 \rightarrow 1$ transitions using an LVG model are shown in Fig. 6. In the $N(^{13}\text{CO})$ map the only conspicuous feature corresponds to the central position ($8 \times 10^{16} \text{ cm}^{-2}$), while in the $N(\text{C}^{18}\text{O})$ map the highest column densities trace the “C” feature (the annulus is included in the $1.5 \times 10^{15} \text{ cm}^{-2}$ contour). The $n(\text{H}_2)$ values obtained from ^{13}CO are more or less homogeneous with an average value of 1750 cm^{-3} . The LVG calculations show that ^{13}CO is optically thick almost everywhere (towards the core $\tau_{10} \geq 3$ and $\tau_{21} > 6$). Thus the derived $n(\text{H}_2)$ value corresponds to the mean volume density of the cloud envelope around the C^{18}O core. In contrast to ^{13}CO , the $n(\text{H}_2)$ volume densities obtained from C^{18}O are very inhomogeneous with values varying from $3 \times 10^3 \text{ cm}^{-3}$ to $5 \times 10^4 \text{ cm}^{-3}$ with an average value over the core of $1 \times 10^4 \text{ cm}^{-3}$.

We estimated the total cloud mass by summing $N(\text{C}^{18}\text{O})$ and $N(^{13}\text{CO})$ over the area and assuming $N(\text{H}_2)/N(\text{C}^{18}\text{O}) = 7 \times 10^6$ and $N(\text{H}_2)/N(^{13}\text{CO}) = 10^6$ (Herking et al. 1982) (corresponding to $N(\text{H}_2)/N(^{12}\text{CO}) = 1.4 \times 10^4$ and $^{12}\text{C}/^{13}\text{C} = 70$ (Langer and Penzias 1990)). The whole cloud mass using ^{13}CO is equal to $5300 M_\odot$ for an area of 2900 arcmin^2 . In the area covered by C^{18}O (650 arcmin^2) we obtained 2700 and $950 M_\odot$ from ^{13}CO and C^{18}O respectively. This latter value of $950 M_\odot$ is very close to the

value derived by Lada et al. (1974) using NH_3 observations, but this is certainly accidental since their mass was derived from a uniform density sphere of $15'$ (1.5 pc) diameter while our mass corresponds to a column density integrated over an area 4 times larger.

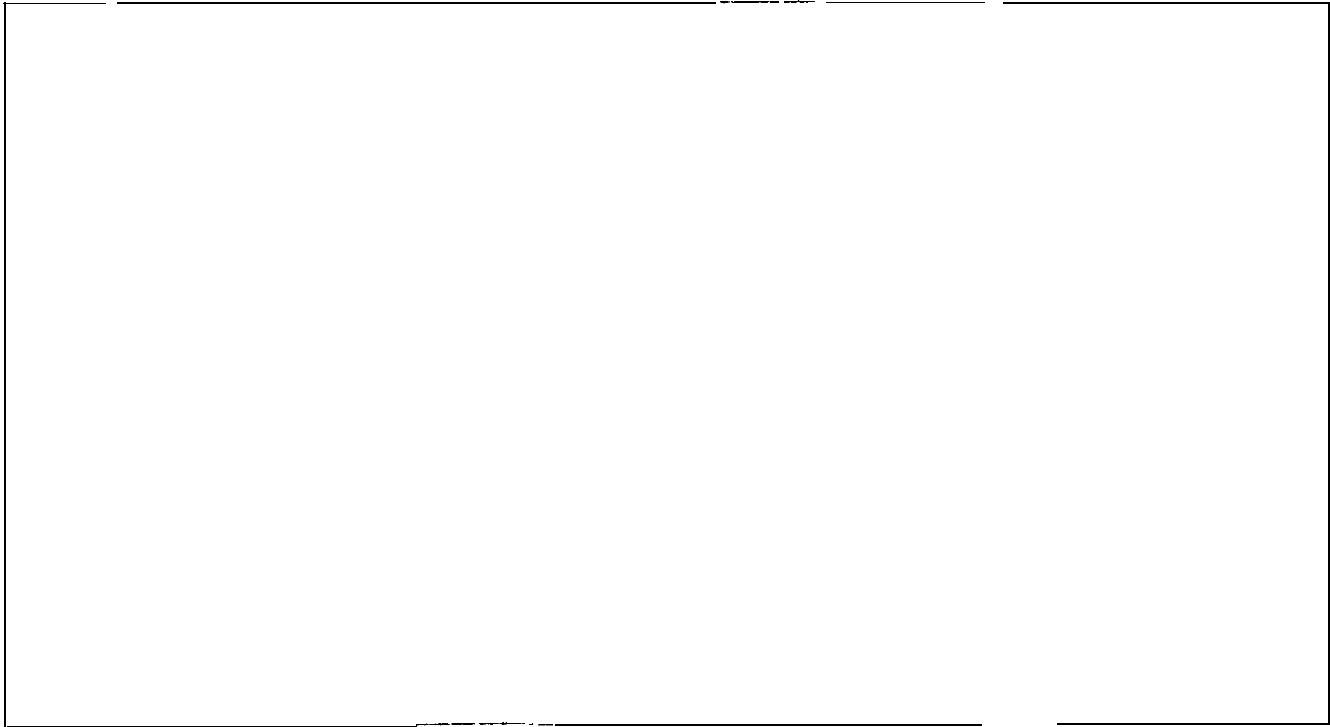


Fig. 6. Left: ^{13}CO column density map of the NGC1333 cloud obtained from the $J=1\rightarrow 0$ and $J=2\rightarrow 1$ transitions of ^{13}CO , using an LVG model. Contours corresponding respectively to $3 \cdot 10^{15}$, $4.5 \cdot 10^{15}$, $6 \cdot 10^{15}$, $8 \cdot 10^{15}$, $1.15 \cdot 10^{16}$, $1.6 \cdot 10^{16}$, $2 \cdot 10^{16}$, $3 \cdot 10^{16}$, $4.5 \cdot 10^{16}$, $6 \cdot 10^{16}$ and $8 \cdot 10^{16} \text{ cm}^{-2}$. Positional offsets in arcminutes are relative to the same center as in Fig. 1. Right: C^{18}O column density map obtained in the same conditions as the left figure. Contours corresponding respectively to $3 \cdot 10^{14}$, $4 \cdot 10^{14}$, $5 \cdot 10^{14}$, $6 \cdot 10^{14}$, $8 \cdot 10^{14}$, $1 \cdot 10^{15}$, $1.25 \cdot 10^{15}$, $1.6 \cdot 10^{15}$, $2 \cdot 10^{15}$, $2.5 \cdot 10^{15}$ and $3 \cdot 10^{15} \text{ cm}^{-2}$.

4. Discussion

In this section we discuss the properties of the fragments, “C” shell, and cavity and their relationship to the dynamics of the core of NGC1333. The dynamics is consistent with a picture of sequential and ongoing star formation.

4.1. Fragmentation structure

As we can see on the maps, the fragmentary structure is more pronounced in C^{18}O than ^{13}CO . As the C^{18}O data are optically thin, they provide a picture of the internal structure and mass distribution. Here we identify the individual clumps and fragments which make up the core structure and estimate their physical properties. As the spatial and velocity resolutions and sampling are better in $\text{C}^{18}\text{O } J=1+0$ than $\text{C}^{18}\text{O } J=2+1$ we have identified the location and size of the clumps using this transition.

First we define the method used to extract the clumps from the $\text{C}^{18}\text{O } J = 1 \rightarrow 0$ data cube. The results can change from one method to another, especially for distinguishing between two clumps which are close in velocity and space. We constructed integrated intensity maps over velocity intervals of 0.5 km s^{-1} covering the velocity range 3 to 10 km s^{-1} . From these maps, we identified the intensity peaks which are spatially separated and greater than three times the noise. For each peak, we located its spatial coordinates α and δ and we drew a spatial-velocity map at constant α and δ to determine the exact position of each clump and to verify if there was more than one clump at the same position but at different velocities. To separate two clumps which are close in velocity and space, the minimum between them must be sufficiently deep so as not to be confused by random noise fluctuations. We considered that two clumps are separated if the minimum between them is lower than the half intensity of the smaller peak. Once the position was known, we determined the velocity width (FWHM) and velocity range (velocity extent over which we see the clump as measured near the baseline). For this, we averaged the 9 spectra which include the central position and the 8 positions around the maximum. The line width is determined from this average spectrum by fitting a gaussian. In the case where we have two clumps, we fitted a double gaussian, with two different velocities. To determine the velocity range for simple and complex features we have used the interval over which the signal is greater than 1σ for a gaussian fit. In the case of a single peak feature the velocity range is straightforward to derive from the average spectrum. In the case where we have a double gaussian fit, we treat each clump separately, and define the velocity range as the 1σ limit at high and low velocities for each gaussian fit. We found that this method gives a more precise value for the velocity interval for each clump than using the spatial-velocity map.

The size of the clump is determined from the integrated intensity map with the area given by the contour at half maximum. Two spatial peaks with the same velocity component and velocity dispersion which are spatially close are considered as separate clumps unless the integrated intensity drops below 50% of the lower of the two maxima at the point between them. Otherwise, we considered that there is only one clump whose position is the center between the two peaks. The size, the velocity dispersion of the clumps and the spatial and velocity separation between two clumps are limited by the spatial ($100''$) and velocity (0.14 km s^{-1}) resolution. The average channel to channel rms noise is another limiting criterion to the detection and separation of clumps.

After identifying the clumps we determined their area and mass. Their area A (in arcmin^2) is given by the contour at half maximum. Then, the deconvolved mean angular diameter is obtained by assuming that their brightness temperature is gaussian. The intrinsic full width half maximum diameter of the clump is obtained by deconvolving the angular diameter assuming a $100''$ FWHM beam and is equal to $\theta_c = \sqrt{4A/\pi - 100^2}$. We convert these diameters to parsecs assuming a distance of 350 pc and list the corresponding radii in table 1.

To derive the clump masses, we sum the $N(\text{C}^{18}\text{O})$ column density over the projected area of the core and convert into hydrogen mass using the $\text{Hz}/\text{C}^{18}\text{O}$ conversion ratio given in section 3. The mass then corrected for the mean mass per particle (mainly due to Helium) by a factor of 1.4. We calculated the virial mass using the formula $M_{\text{vir}} = 126 \times \delta v^2 \times R$ (Mac Laren et al. (1988)) which assumes a density distribution in $1/r^2$. The virial and luminosity masses are tabulated in table 1 and plotted in Fig. 7.

Table 1. Properties of C^{18}O clumps

Number	RA offsets	Dec offsets	VLSR (km s ⁻¹)	Δv (km s ⁻¹)	area (arcmin ²)	R_c^a (pc)	Mass (M_\odot)	M_{vir}^b (M_\odot)
<1	-1	-35	5.70	0.60	12	0.18	10	8.2
2	-2	-31	6.20	0.60	23	0.26	15	11.8
3	-7	-26	5.90	1.10	48	0.39	40	59.5
4	-6.5	-20.5	6.75	1.25	20	0.24	25	47.2
5	-2	-14	7.08	1.90	26	0.28	70	127.4
6	-5	-9.5	6.60	1.05	18	0.23	25	32.0
7A	10.5	-13.5	6.85	1.00	18	0.23	25	29.0
7B	10.5	-14	8.20	0.90	12.5	0.18	20	18.4
8	0	-7.0	7.50	1.87	45	0.37	125	163.0
9	7.0	-11.0	7.54	1.25	25	0.27	40	53.2
10A	3.0	-2.0	6.75	1.50	16.5	0.22	40	62.4
10B	2.0	-3.0	8.60	1.36	23	0.26	10	60.6
11	1.0	1.0	7.73	1.73	40	0.35	120	132.0
12	3.5	5.0	7.48	0.80	34	0.32	60	25.8
13	-14.0	7.0	7.97	1.00	23	0.26	40	328
14	-4.0	9.0	7.93	1.00	10	0.16	20	20.2

^a The radius is calculated as mentioned in §4.1 and assuming a distance of 350 pc

^b The virial mass M_{vir} is calculated using the formula $M_{vir} = 126 \times \delta v^2 \times R$ for $1/r^2$ density dependence

The total mass of the cloud obtained from C^{18}O is $950 M_\odot$ for an area surveyed of 650 arcmin^2 (cf Section 3.3). Of these $950 M_\odot$, we calculated that $745 M_\odot$ are in the 16 clumps extracted from our data, covering a surface of 280 arcmin^2 . This means that on average the density in the cores is increased by a factor of three. Furthermore inside the elliptical core defined from the C^{18}O map, we find 6 clumps out of 16 representing $450 M_\odot$ (60% of the mass of all the clumps) within an area of 140 arcmin^2 . This represent an increase in the mean density of a factor of 5 in the clumps compared to the average density of the total core and a factor of 9 compared to the average density of the gas outside the cores. This latter value is consistent with our estimate of density from the CS excitation.

In Fig. 8 we plot the log of the luminosity mass versus the log of the virial mass. We plot the line for $M_{vir} = M_L$ for $1/r^2$ density dependance. For a mass greater than M_{vir} the clumps are unstable against gravity and should collapse, while for clumps with $0.5 M_{vir} \leq M \leq M_{vir}$ the clump is in equilibrium and stable against collapse. Finally for masses less than $0.5 M_{vir}$ the clumps are unbound and should expand and dissipate. Within the uncertainty of the mass estimate (a factor of 2) and the uncertainty on the virial mass estimate due to the density profiles, half of the objects appear unstable and will collapse and the other half appear to be bound but stable. objects.

4.2. Dynamics of the core

As derived in the results section we see in the central region of our C^{18}O and CS maps the presence of a “C” shell and a cavity. Part of this shell can also be seen in the NH_3 map of Ho and Barrett (1980) (see Fig. 9). This shell is the location of the three largest molecular subcores traced by C^{18}O , several far and near-infrared sources (Jennings et al. 1987, Sandell et al. 1991), and numerous Herbig-Haro objects. Most of the far-IR (IRAS) sources have associated optical or near-IR objects and outflows. The most conspicuous outflow is the one originating from the cluster of sources SSV13 situated on the inside of the cavity, with both



Fig. 7. Position and luminosity masses of the C^{18}O clumps listed in table 1 (masses are proportional to the circle radius) superimposed on the integrated velocity map for the $J = 1 \rightarrow 0$ transition of C^{18}O (Fig. 2)

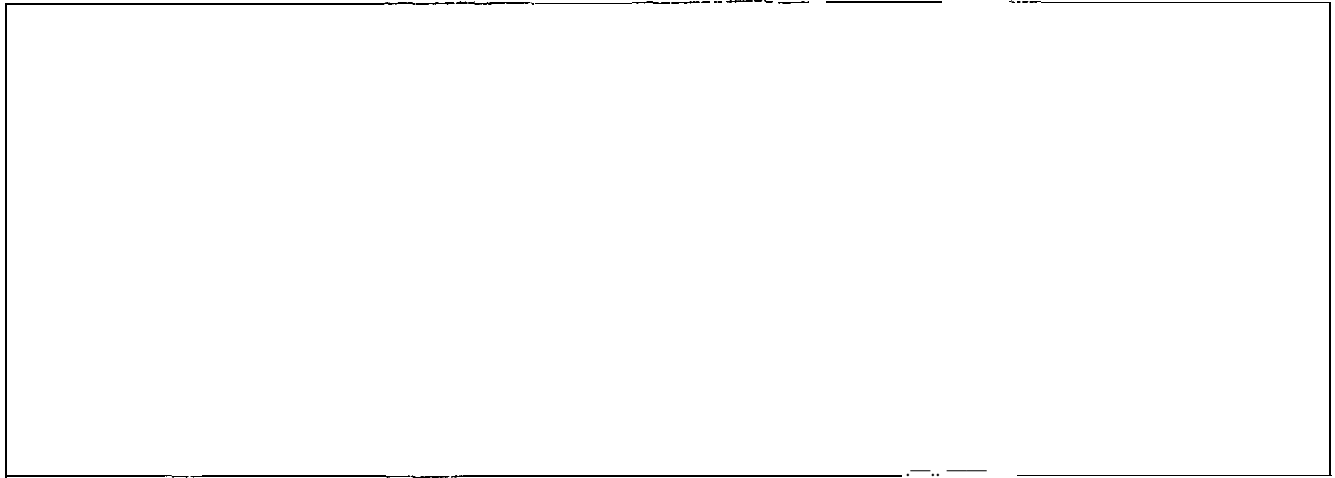


Fig. 8. Log of the luminosity mass (M_L) versus the log of the virial mass (M_{vir}). On the same figure we have plotted the line for $M_{\text{vir}} = M_L$ for $1/r^*$ density dependence

high velocity (terminal velocity of 27 km s^{-1} (Snell and Edwards 1981)) and extremely high velocity outflow (terminal velocity of 160 km s^{-1} (Bachiller and Cernicharo 1990)). The direction of this outflow is perpendicular to the side of the cavity and its red lobe fills almost entirely the cavity while the blue lobe, which includes the HH7-11 objects, impact into the surrounding shell (see Fig. 9). The kinetic energy associated with this outflow ($\sim 6 \times 10^{45}$ ergs according to Bachiller and Cernicharo (1990)) is large enough to have emptied the cavity of its original mass. A second outflow associated with HH 12 at position $(-1', 0')$ and driven by the nearby SSV12 star was discovered by Edwards and Snell (1983j). It is situated in the northern part of the cavity, has

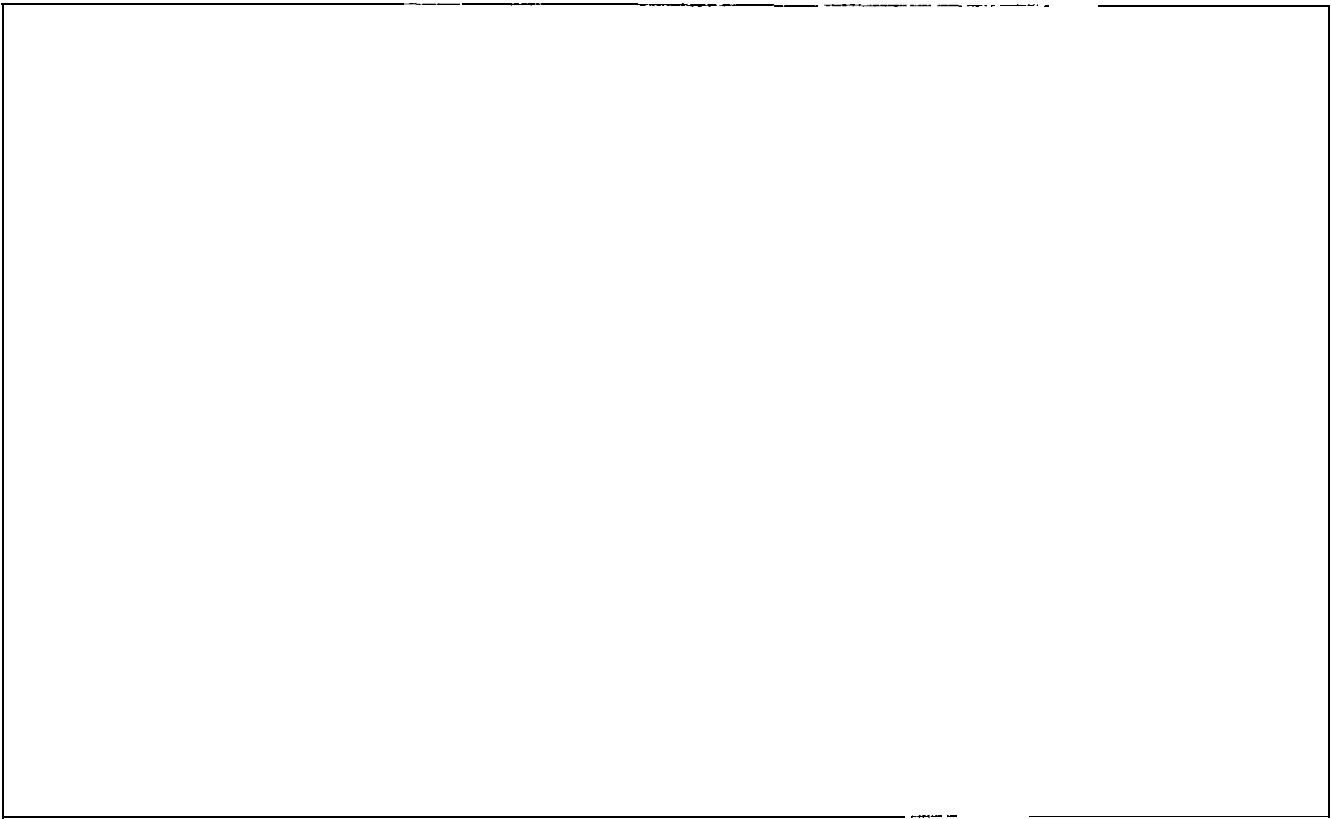


Fig. 9. Left : Superposition of the NH_3 map (adapted from Ho and Barrett 1980) and the $\text{C}^{18}\text{O } J=1 \rightarrow 0$ integrated velocity map (limited to the “C” shell). We have superimposed the IRAS infrared sources (filled circles) and the infrared sources with optical counterparts (filled squares). Right : Superposition of the red and blue lobes of the SSV 13 outflow on the $\text{C}^{18}\text{O } J=1 \rightarrow 0$ integrated velocity map. The position and direction of the IRAS2, IRAS4, IRAS7 and SSV12 outflows are also indicated by stars and thick arrows (see section 4.2). Note that in IRAS2 two outflows with perpendicular directions have been detected (see section 4.2)

a N-S direction with its red lobe merging to the south into the SSVI 3 red outflow. In addition three other sources with weaker CO molecular outflows were discovered in this shell (Liscau et al. 1988; Aspin and Sandell 1991). The driving sources for these outflows are also situated near the wall of the cavity. One of these sources is IRAS2 situated at position $(-1', -5.7')$ in our maps. This source drives two outflows (Sandell et al. 1994): a N-S outflow previously discovered by Liscau et al. (1988) which merges into the SSVI 3/HH7-11 outflow and an E-W outflow, perpendicular to the eastern wall of the cavity, which looks like a molecular jet. These two outflows have very different dynamical timescales (2.5×10^4 yr for the N-S flow and 6×10^3 yr for the E-W flow) which Sandell et al. show to originate from two sources which formed in close proximity. Sandell et al. (1994) discovered at the termination of the young red lobe (to the west of IRAS2) a strong enhancement in the $\text{CS } J=5 \rightarrow 4$ and methanol lines proving that this outflow is entering into the much denser gas of the “C” shell. This strong CS emission near IRAS2 explains the presence of the very bright $\text{CS } J=2 \rightarrow 1$ spot in our maps. We have used the $\text{CS } J=5 \rightarrow 4$ from Sandell et al. along with our $\text{CS } J=2 \rightarrow 1$ to determine from an LVG excitation analysis that the density in this CS spot is greater than a few $\times 10^5 \text{ cm}^{-3}$. Another outflow was discovered around IRAS4 (position $(2.3', -6.7')$ in our maps) by Sandell et al. (1993). This outflow is driven by the IRAS4A source which seems to be the youngest protostar yet found. Finally, the IRAS7 outflow, has been discovered by Liscau

et al (1988) and fully mapped in $\text{CO } J = 3 \rightarrow 2$ by Sandell et al (1993). Its direction is also perpendicular to the wall of the cavity. Of particular interest are the densest parts of the three subcores seen in the “C” shell. Their luminosity masses determined from C^{18}O are approximately 50, 30 and $40 M_{\odot}$ (going from north to south) and these are close to the virial masses of these objects. It appears very likely that these three clumps are unstable (or nearly unstable) to gravitational collapse.

We have estimated the kinetic energy necessary to remove the material surrounding the star and compared this result with the mechanical energy produced by the outflows. Because the outflow has compressed all the material in the “C” shell which originally existed inside the cavity, the total mass of the “C” shell should represent the mass of the original spherical cloud. Using the full resolution $\text{BL } \text{C}^{18}\text{O } J = 1 \rightarrow 0$ map we estimated the C^{18}O column density at each point of the “C” shell using the velocity integrated intensity of the line together with an excitation temperature estimated from our LVG calculations at lower resolution. We obtain a total mass of $200 M_{\odot}$. The mean density of the original material was estimated assuming that the initial volume which contained this mass was a hemisphere with a 6' radius (0.6 pc), leading to $n(\text{H}_2) = 5500 \text{ cm}^{-3}$. Consequently the original mass inside the cavity (radius $\sim 3'$ (0.3 pc)), excluding that converted to young stellar object, was $22 M_{\odot}$. The energy to create the cavity, that is to move the material to the inner edge of the shell is a few 10^{43} ergs, which is much smaller than the energy available from the outflows. Because the gas from the cavity has also been accelerated to 6 km s^{-1} as estimated from the velocity measured in the SSV13 outflow (Bachiller and Cernicharo 1990), we would require 8×10^{44} ergs to empty the cavity and accelerate the gas. The presence of all the outflow sources, including SSV13, indicate that there is more than enough energy to create the cavity, accelerate the gas and compress the shell.

From the properties of the cavity, the C shell and the embedded sources described above we propose an evolutionary scenario for the core of NGC1333. First we suggest that SSV13 was among the first sources to form in the core (according to Bachiller and Cernicharo (1990) it was formed more than 104 years ago). The outflow from this source would have swept up and compressed the surrounding material creating a small cavity and initiating a second stage of star formation (IRAS2, IRAS4) in a compressed shell. We further suggest that the outflow from the second generation of young stellar objects swept up more material, creating the larger cavity seen presently and compressing the gas further. The dense clumps seen in the C shell may be the sites for the next generation of star formation in NGC1333.

5. Summary

We have mapped the molecular core of NGC1333 in ^{13}CO and $\text{C}^{18}\text{O } J = 1 \rightarrow 0$ and $J = 2 \rightarrow 1$ and $\text{CS } J = 2 \rightarrow 1$ to determine its structural properties and relationship to the embedded young, stellar objects and outflows. We find:

1. The core of NGC1333 as traced by C^{18}O appears to have a large cavity (radius of 0.3 pc), surrounded by a shell of gas (outer radius 0.6 pc) which is currently undergoing compression. This shell in projection on the sky has a prominent “C” shape.
2. It seems that the outflow from SSV13, IRAS2 and IRAS4 are responsible for creating the cavity and compressing the shell.
3. The total mass of the core as traced by C^{18}O is $450 M_{\odot}$ of which $360 M_{\odot}$ is in the shell. Three to four condensed fragments are found in this shell having masses in the range $80\text{--}120 M_{\odot}$.

4. The dense massive fragments in the shell are gravitationally unstable to collapse and are likely sites of the next generation of star formation in NGC 1333.
5. One of the fragments located in the S-E of the shell is the brightest source of $\text{CS } J = 2 \rightarrow 1$ emission and has strong $\text{CS } J = 5 \rightarrow 4$ emission. It is located at the position where the blue outflow lobes of SSV13 and the “young” red lobe of IRAS2 are impinging on the cavity wall. This fragment may be driven into gravitational collapse by this shock compression.

In conclusion the age of the outflow sources and their location inside a cavity, but close to its wall, suggests that the core of NGC 1333 may be undergoing sequential star formation driven by winds sweeping up material and shock compressing the gas,

Acknowledgements. We would like to thank Dr. Gilles Duvert of Grenoble Observatory for his help with the POM-2 observations and the reduction of data. We would also like to thank Dr. Greg Wright of AT&T Bell Laboratories for his help with the 7m observations. WDL would like to thank the University of Grenoble for hospitality during several stages of this work. The research of WDL was carried out under the LTSA program by the Jet Propulsion Laboratory, California Institute of Technology, under contract with the National Aeronautics and Space Administration.

References

- Aspin C., Sandell G., 1991, The JCMT Newsletter, No 1, 21
 Aspin C., Sandell G., Russell A. P. G., 1994, A&AS, 106, 165
 Bachiller R., Cernicharo J., 1986, A&A 166, 283
 Bachiller R., Cernicharo J., 1990, A&A 239, 276
 Bally J., Stark A. A., Wilson R., 1987, ApJS 65, 13
 Borgman J., Blaauw A., 1964, Bull. Astron. Inst. Netherlands 17, 358
 Bregman J., Rank D., Sandford S. A., Termini F., 1993, ApJ 410, 668
 Castellet M. W., Hackwell J. A., Grasdalén G. L., Gehr R. D., 1986, ApJ 300, 406
 Castets A. et al, 1988, (POM2), A&A 194, 340
 Castets A. et al, 1990, A&A 234, 469
 Cernicharo J., Bachiller R., Duvert G., 1985, A&A 149, 273
 Dent W. R. F. et al, 1993, MNRAS 262, 1.13
 Edwards S. and Snell R. L., 1983, ApJ 270, 605
 Edwards S. and Snell R. L., 1984, ApJ 281, 237
 Flower D. R. and Launay J. M., 1985, MNRAS 214, 271
 Frerking M. A., Langer W. D., Wilson R. W., 1982, ApJ 262, 590
 Gezari D. Y., Schmitz M., Pitts P. S., Mead J. M., 1993, Catalog of infrared observations: I ar Infrared Supplement ($\lambda \geq 6\mu\text{m}$), NASA Reference Publication 129S
 Harvey P. M., Wilking B. A., Joy M., 1984, ApJ, 278, 156
 Ho P. T. P., Barrett A. H., 1980, ApJ 237, 38
 Jennings R. E., Cameron D. H. M., Cudlip W., Hirst C. J., 1987, MNRAS 226, 461
 Lada C. J., Gottlieb C. A., Litvak M. M., Lilley A. E., 1974, ApJ 194, 609
 Ladd E. F., Lada E. A., Myers P. C., 1993, ApJ 410, 168
 Langer W. D., Wilson R. W., Goldsmith P. F., Beichman C. A., 1989, ApJ 337, 355
 Langer W. D., Penzias A. A., 1990, ApJ 357, 477
 Liseau R., Sandell G., Knee L. B. G., 1988, A&A 192, 153
 Liseau R., Lorenzetti D., Molinari S., 1992, A&A 253, 119
 Lizano S. et al, 1988, ApJ 328, 763
 Loren R. B., 1976, ApJ 209, 466
 Mac Laren I., Richardson K. M., Wolfendale A. W., 1988, ApJ 333, 821
 Phillips J. I., Mampaso A., 1990, Ap&SS 171, 189
 Reipurth B., 1994, A General Catalogue of Herbig-Haro Object, Electronic Version
 Sargent A. I., 1979, ApJ 233, 181
 Sandell G., Aspin C., Duncan W. D., 1991, ApJL 376, 1.17
 Sandell G., Aspin C., 1993, The JCMT Newsletter, No 1, 43
 Sandell G., Knee L. B. G., Aspin C., Robson J. E., Russell A. P. G., 1994, A&A 285, L1
 Schwartz P. R., Bologna J. M., Waak J. A., 1978, ApJ 226, 469
 Schwartz P. R., Waak J. A., Smith H. A., 1983, ApJL 267, 1.109

- Snell R.L. and Edwards S., 1981, *ApJ* 251, 103
- Strom S.E., Grasdalen G. L., Strom K. M., 1974, *ApJ* 191, 111
- Strom S. E., Vrba F. J., Strom K.M., 1976, *AJ* 81, 314
- Strom K. M., Margulis M., Strom S. E., 1989 *ApJL* 345, 1, 79
- Ungerechts 11., Thaddeus 1', 1985, *ApJS* 63, 645

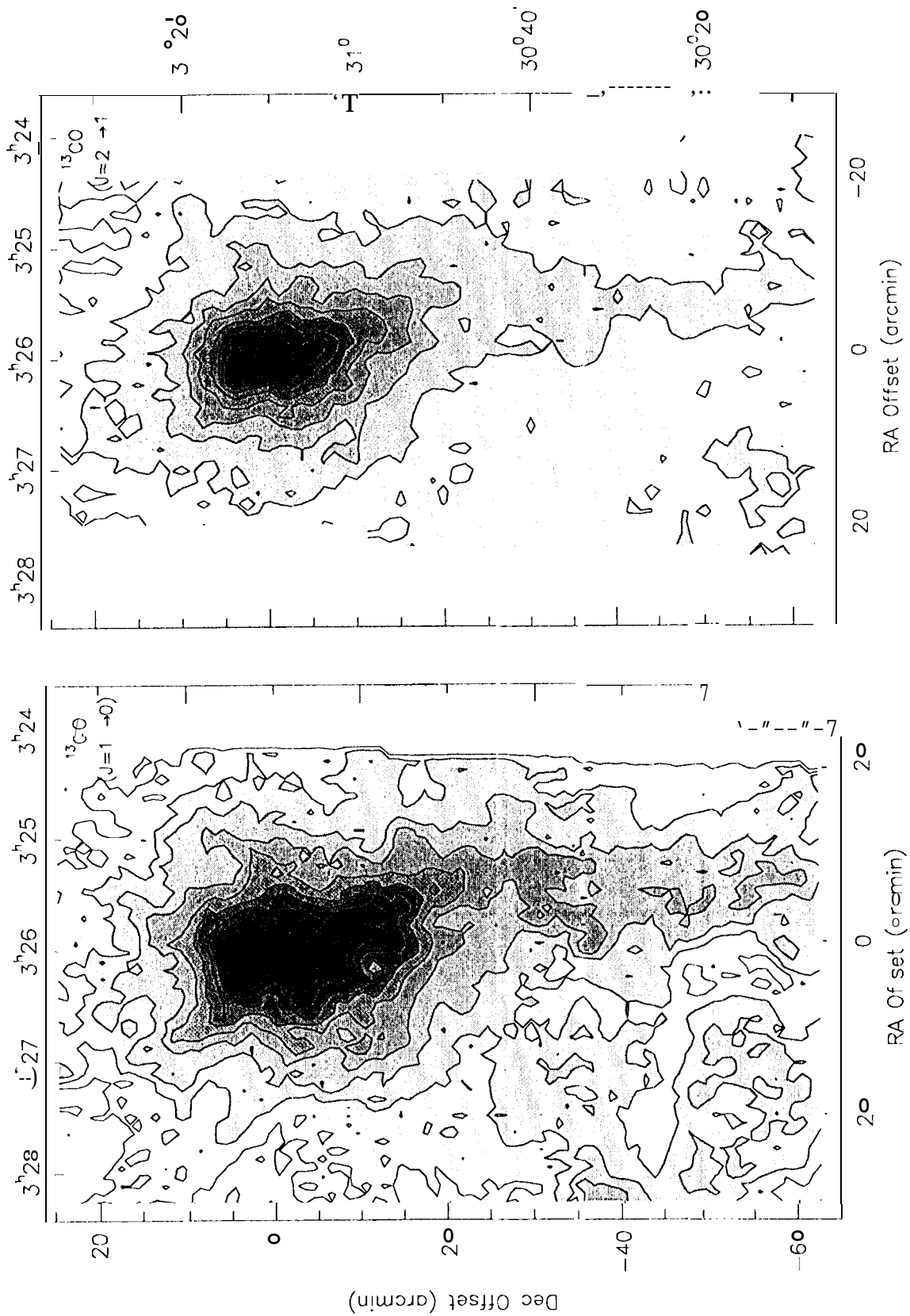


Fig 2.

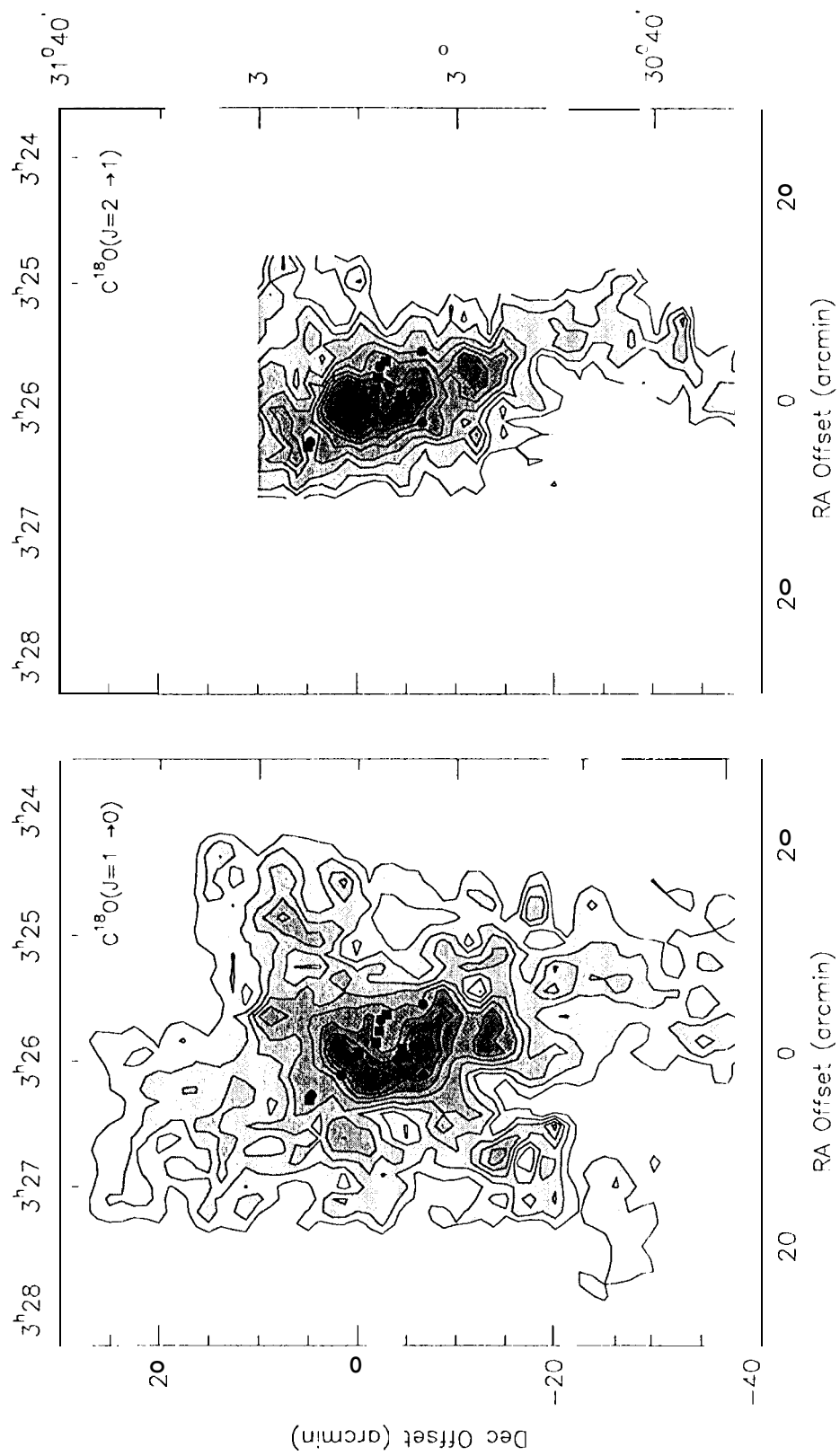


Fig. 2

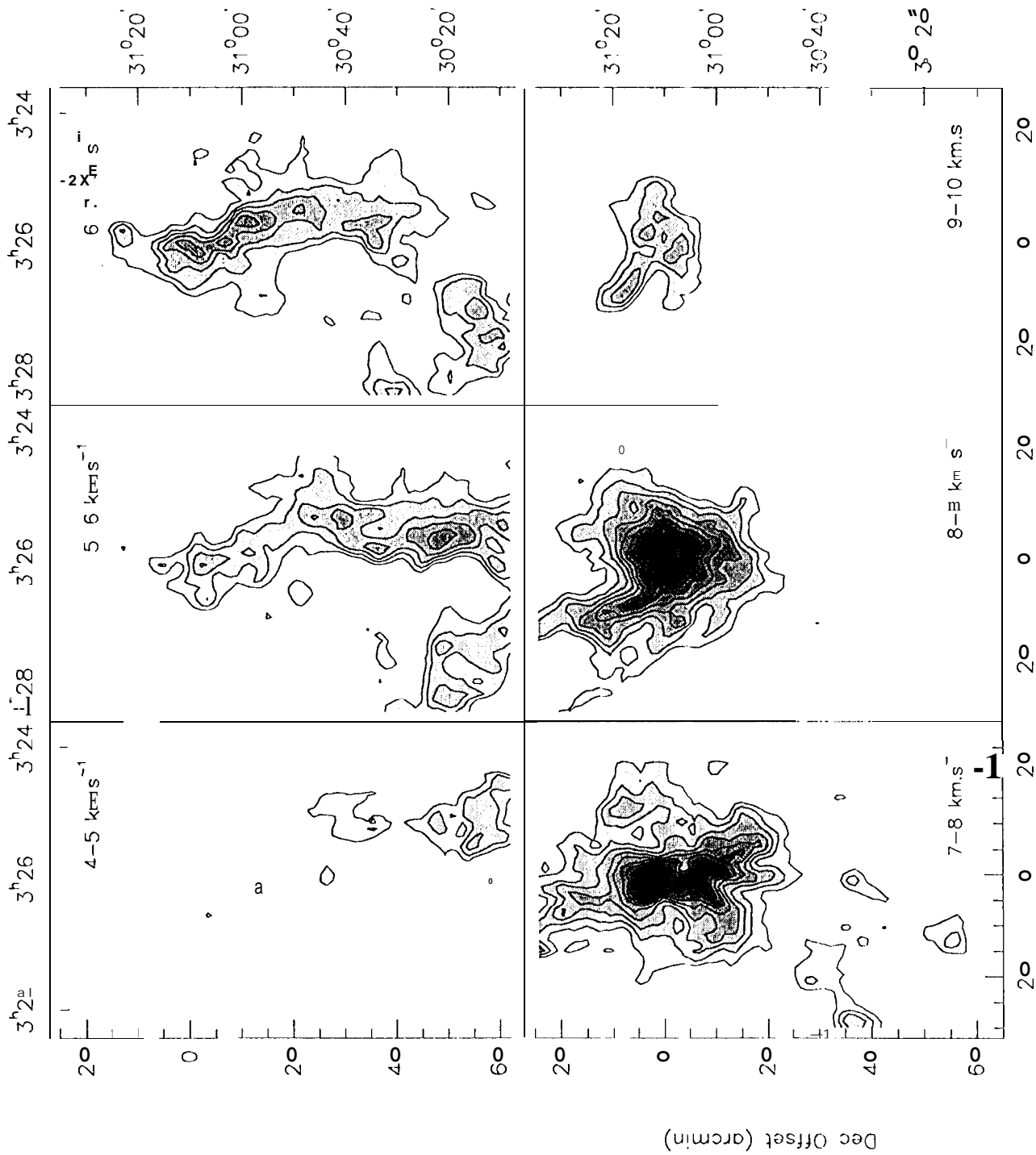


Fig. 3

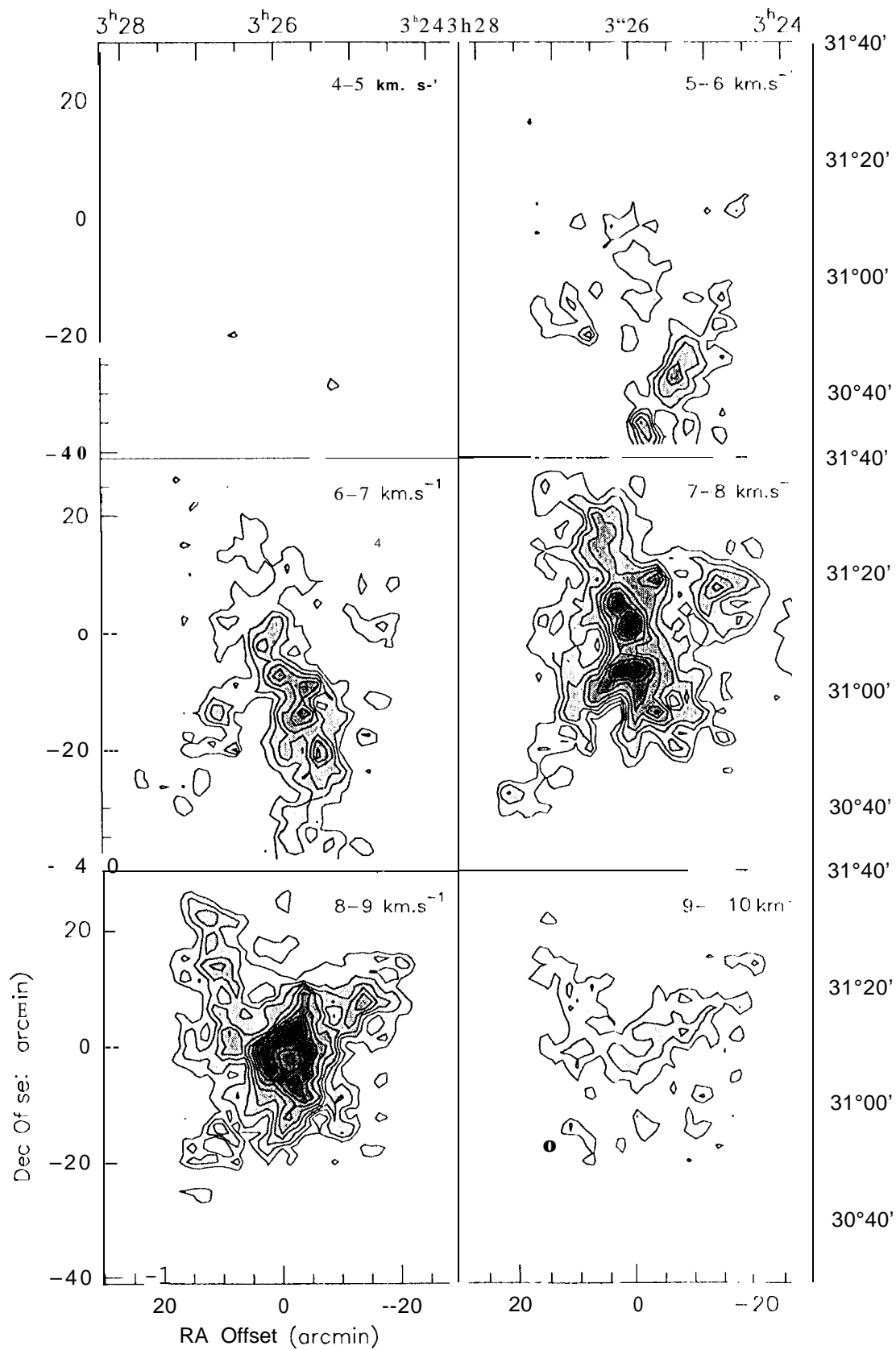


Fig. 4

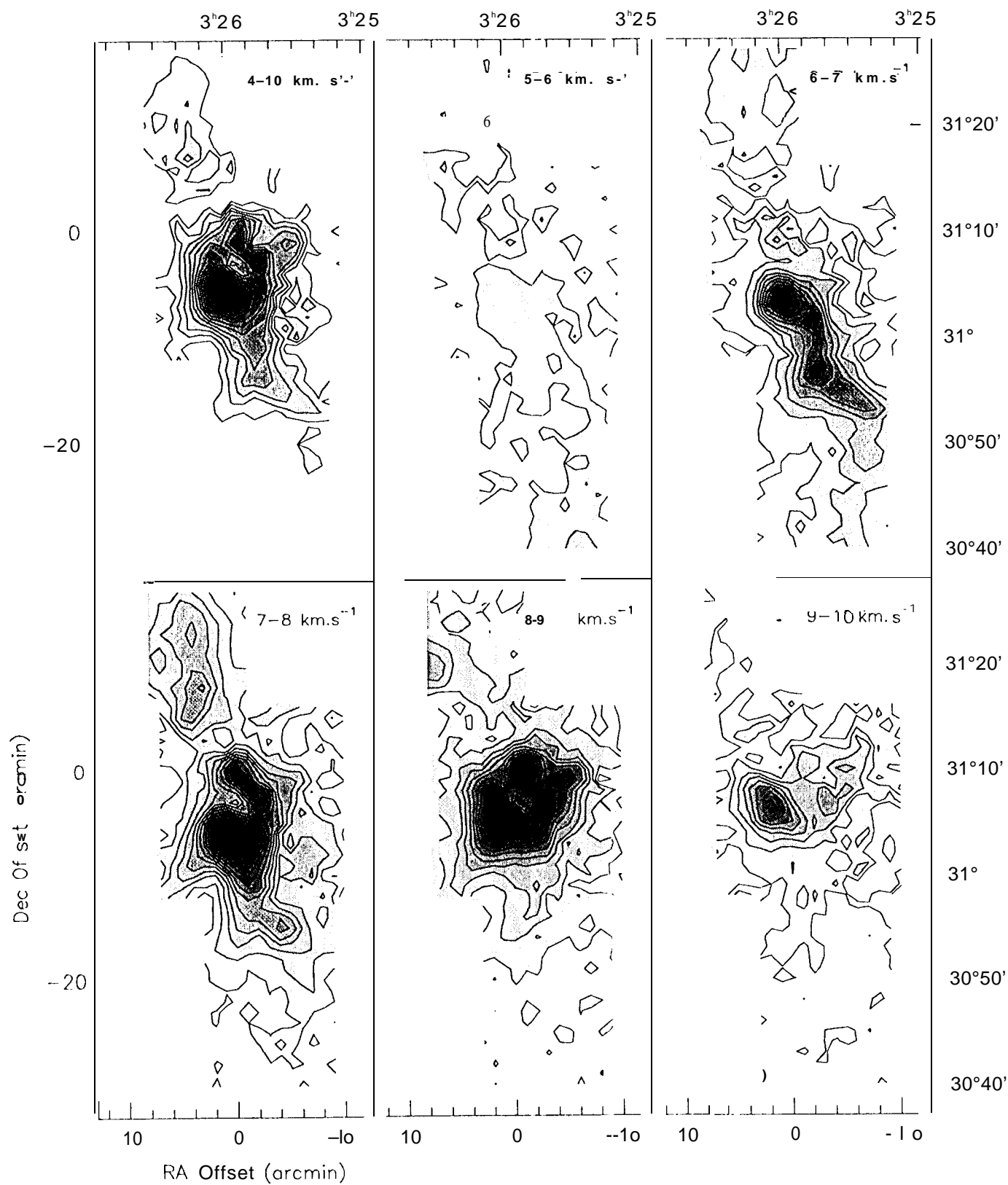


Fig. 5

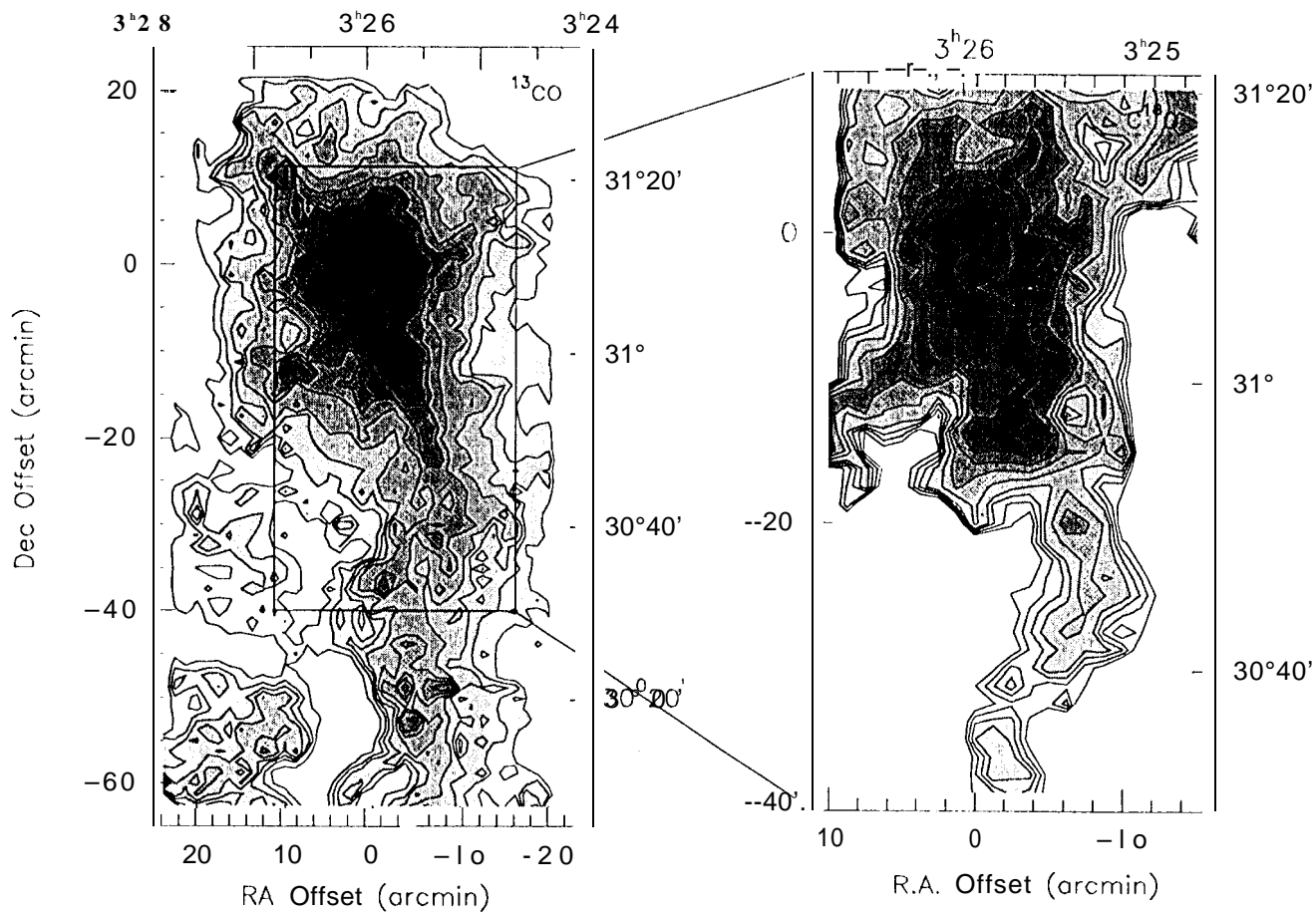


Fig. 6

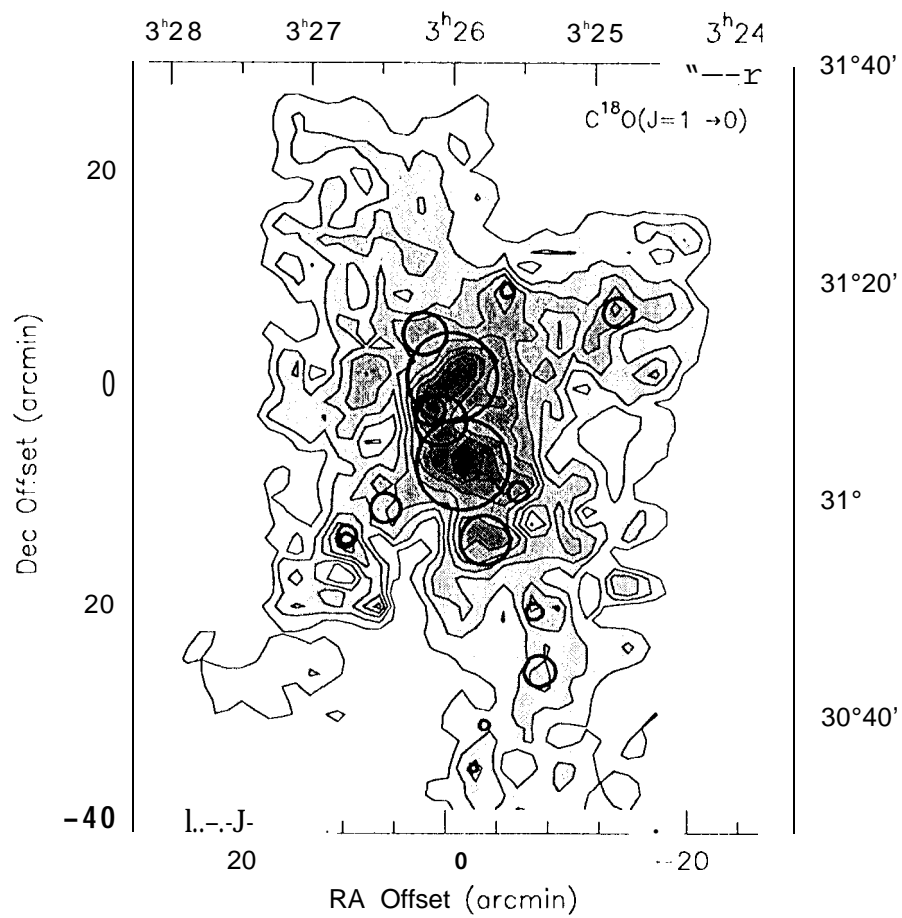


Fig. 7.

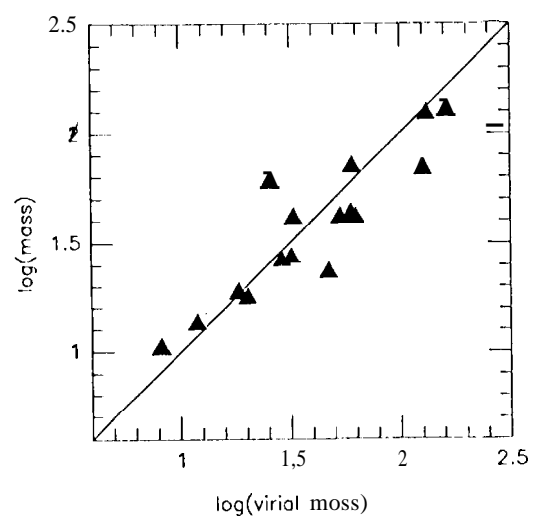


Fig. 8 .

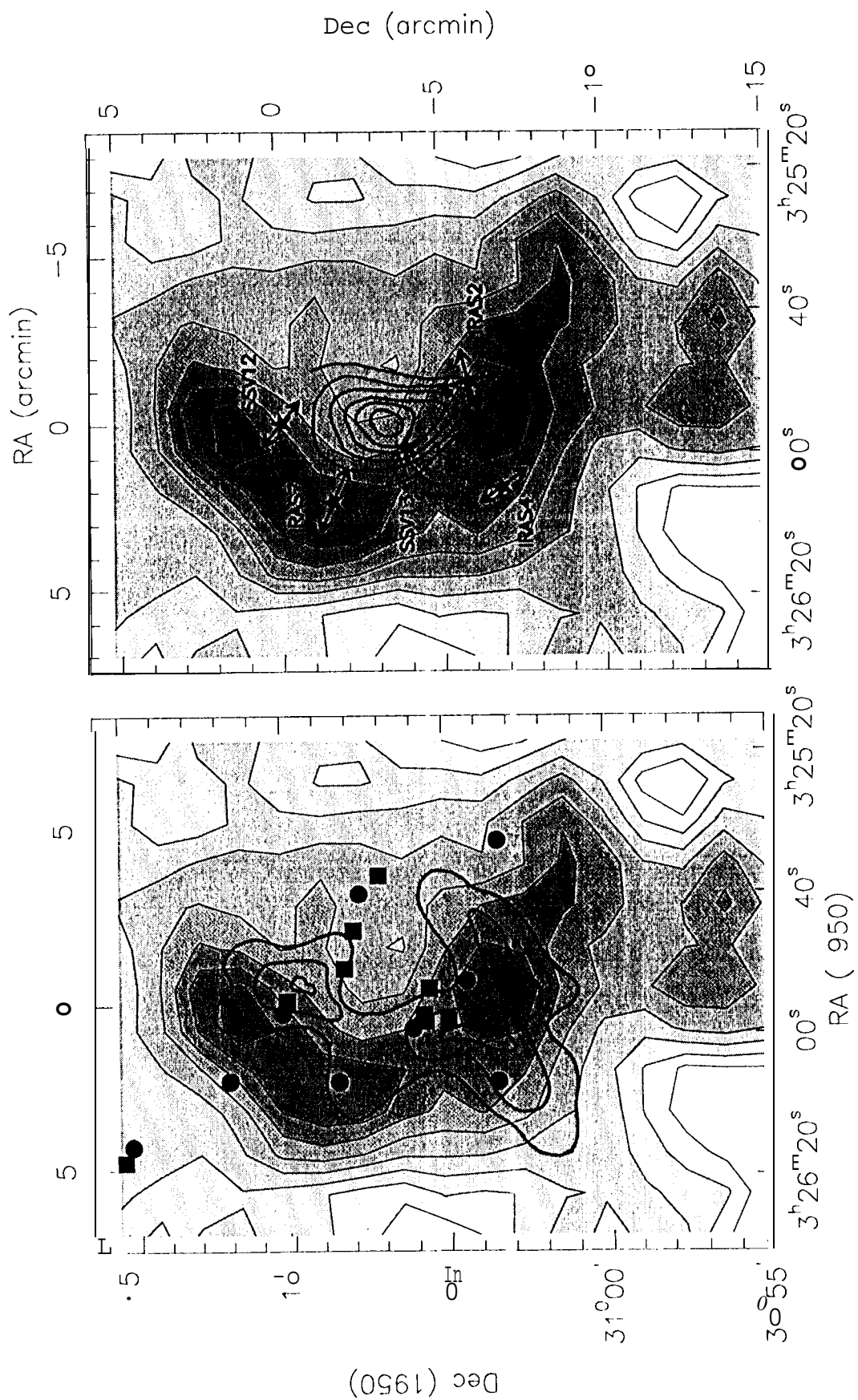


fig. 9